CHEMISTRY OF MATERIALS

pubs.acs.org/cm

Article

Viable Metal–Organic Framework Adsorbents for Thermodynamics-Driven Methane/Hydrogen Separation

Prantar Dutta, Adriano Henrique, Writakshi Mandal, Laura Bueno, Rosana V. Pinto, Yann Magnin, Sandra Barbouteau, Georges Mouchaham, Christian Serre, José A. C. Silva,* and Guillaume Maurin*

Cite This: *Chem. Mater.* 2026, 38, 5438–5452

Read Online

ACCESS | Metrics & More | Article Recommendations | Supporting Information

ABSTRACT: Hydrogen is a clean energy carrier that supports low-carbon mobility and power generation and is widely used in oil refining and methanol production. Efficient separation of methane (CH_4) from hydrogen (H_2) is critical in the hydrogen supply chain, particularly for H_2 purification after steam methane reforming and H_2 recovery from natural gas pipelines. In this work, atomistic simulations were employed to systematically evaluate a diverse set of existing metal–organic frameworks (MOFs) for physisorption-based CH_4/H_2 separation under realistic pressure swing adsorption (PSA) conditions. The selected MOFs combine favorable chemical and geometrical features with practical advantages including synthetic feasibility, stability, environmental sustainability, and scalability. Force field Monte Carlo simulations were deployed to predict single-component and mixture adsorption isotherms of CH_4 and H_2, as well as their adsorption enthalpies at zero coverage, with the approach validated against experimental adsorption and breakthrough data for selected materials. Several MOFs were predicted to outperform the commercial adsorbent Zeolite 13X, exhibiting superior separation performance in terms of CH_4/H_2 selectivity and CH_4 working capacity. Structure–property analysis revealed key relationships between pore architecture, chemical functionality, and separation performance. Furthermore, molecular dynamics simulations of CH_4 diffusion in the MOF pores confirmed the kinetic suitability of top-performing materials for PSA operation. Overall, this study identifies a set of viable MOFs as promising candidates for efficient CH_4/H_2 separation and provides molecular-level insights to guide the development of hydrogen purification technologies.

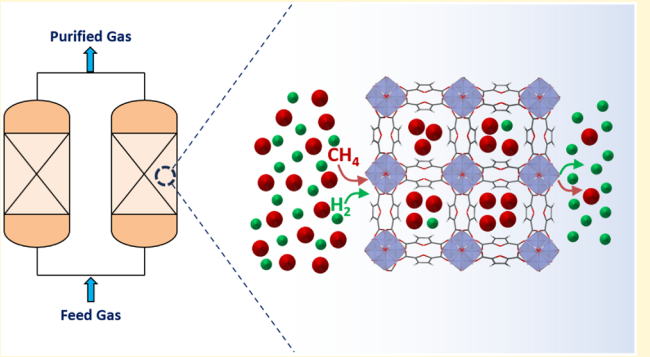

1. INTRODUCTION

The adverse effects of climate change from fossil fuel use have significantly increased the demand for alternative energy sources. As global energy consumption continues to rise, the need for clean and efficient fuels to power various economic sectors becomes more urgent. Hydrogen (H_2) has emerged as a promising sustainable energy option for transportation and electricity generation, offering high specific energy content, releasing only water vapor upon combustion, and being compatible with both internal combustion engines and fuel cells.[1] This energy source is expected to meet 24% of global energy demand by 2050.[2] Currently, about 95% of H_2 is produced via steam methane reforming (SMR),[3] although alternative strategies such as electrolysis powered by renewable electricity and thermochemical water splitting are actively explored.[4] The effluent from SMR still contains unreacted species, mostly methane (CH_4), that need to be removed to obtain high-purity H_2.[3] At present, most of the H_2 produced is consumed in oil refining and the synthesis of ammonia and methanol.[5] Looking ahead, its use is expected to expand into electricity generation and transportation, making it a cornerstone of carbon-neutral energy systems.[2] However, a key barrier for the widespread adoption of H_2 energy systems lies in fuel transportation.[6] Although both liquid and gaseous H_2 can be transported by trucks, rail, and ships, the long transit times and complex infrastructure needs, combined with the energy penalty of liquefaction, make these strategies unfeasible for large-scale, long-distance transport.[7] An increasingly promising alternative is blending gaseous H_2 into existing natural gas pipelines, allowing cotransport with CH_4 over long distances and separation near end-use locations.[8] Previous works have shown that gas mixtures containing 10% to 20% H_2 by volume can be safely transported without major modifications to existing pipeline systems.[9] This solution is economically attractive as it allows H_2 to be conveniently

Received: December 16, 2025
Revised: May 11, 2026
Accepted: May 13, 2026
Published: May 19, 2026

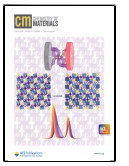

transported to industries and gas stations worldwide without significant investment in new infrastructure.

Hence, both high purity H_2 production from SMR and effective H_2 transport in blended natural gas pipelines for its on-site end use crucially rely on CH_4/H_2 separation. Traditional separation processes, such as cryogenic distillation and chemical absorption, are highly energy-demanding.[10,11] Adsorption- and membrane-based separations using porous solids offer great alternatives.[12] Physisorption-based gas mixture separation in porous media is generally driven by three possible mechanisms: thermodynamic separation, where selective adsorption arises from differences in host/guest interactions and/or confinement effects; kinetics separation, which exploits differences in molecular diffusivities within pores; and molecular sieving, where pore apertures selectively exclude larger molecules.[13] Among these, pressure swing adsorption (PSA), which leverages thermodynamics-driven physisorption, is particularly attractive because it offers low energy consumption, high product purity, and is scalable for large-volume processing.[14] This technology requires porous adsorbents with high CH_4/H_2 selectivity and adequate CH_4 working capacity in the desired pressure range. This separation is highly challenging since both adsorptive species are nonpolar, resulting generally in weak host/guest interactions. Conventional porous sorbents, such as zeolites and carbons have been explored for CH_4/H_2 separation; however, their moderate selectivity limits the applicability of PSA as an alternative to conventional separation processes.[15−19] Hence, there is a need to explore other classes of advanced adsorbents with enhanced performance to tackle the challenges raised by this complex gas mixture separation.

Metal−organic frameworks (MOFs), owing to their highly tunable pore size, surface chemistry, and topology have garnered widespread interest for applications such as gas storage, separation, catalysis, sensing, and drug delivery among others.[20−24] In terms of gas separation, MOFs have been extensively explored for CO_2 capture[25−27] and hydrocarbon separations.[28,29] However, among the more than 140,000 synthesized MOFs so far, only a few, often identified by trial-and-error, have been proposed for CH_4/H_2 separation.[30−34] To overcome this limitation, high-throughput computational screening approaches leveraging molecular simulations and, increasingly, machine learning models have been employed to identify both existing and hypothetical MOFs with attractive CH_4/H_2 separation performance.[35−42] However, the conclusions of these studies have to be considered in light of their inherent limitations: they employed MOF structure databases that are known to contain structural/chemical errors,[43] implemented simplified workflows such as the assessment of ideal selectivity based on single-component sorption data, and frequently proposed candidates that are not viable for industrial use. Indeed, for MOFs to be practical adsorbents in PSA systems, various factors including the cost and availability of precursors, mechanical and thermal stability under process conditions, ease of synthesis and activation, production scalability, toxicity, and sustainability must be considered beyond their attractive adsorption performance.[44−47]

Herein, grand canonical Monte Carlo (GCMC) simulations first systematically assessed CH_4/H_2 separation performance of a series of sustainable and stable existing MOFs and their variants. Two relevant applications have been considered: H_2 purification after SMR (25:75 CH_4/H_2) and H_2 recovery from natural gas grids (90:10 CH_4/H_2). The overall simulation strategy (MOF structure models, adsorbate models, and choice of force field parameters) was first validated against experimental single-component adsorption data and binary breakthrough experiments collected on benchmark Al and Fe microporous MOFs such as MIL-160(Al),[48] MIL-120(Al),[49] and MIL-127(Fe),[50] all synthesized along scalable greener protocols previously reported by some of us. This computational evaluation revealed three categories of MOFs with (i) high CH_4/H_2 selectivity but rather low CH_4 working capacity, (ii) high CH_4 working capacity but relatively low CH_4/H_2 selectivity, and (iii) a balanced combination of both metrics. These overall predictions were rationalized to establish initial structure−property relationships. Finally, to complement the thermodynamic analysis, molecular dynamics (MD) simulations were performed to examine CH_4 diffusion in representative promising MOFs, confirming their kinetics suitability for PSA processes. Overall, this joint computational-experimental study provides a comprehensive framework for identifying effective MOFs for CH_4/H_2 separation, laying the foundation for scalable hydrogen technologies.

2. METHODOLOGY

2.1. MOF Selection and Structure Geometry Optimization

We selected ∼20 MOFs as the initial set of adsorbents with a broad range of pore size, shape and topology, and chemical functionalities including both channel-like and cage-like structures. This selection focused on materials synthesized from abundant, sustainable, and low-cost metals such as Al, Fe, and Zn and with previously reported high thermal and mechanical stability to ensure their practical viability under PSA operating conditions. Additionally, all selected frameworks have pore sizes larger than 3.8 Å, the kinetic diameter of CH_4, to allow molecular access, yet small enough to offer moderate to strong confinement, which is critical for achieving high CH_4 affinity and associated high CH_4/H_2 selectivity. The MOF structures were obtained either from the Cambridge Structural Database (CSD)[51] or from previously published works. All structures were manually curated to ensure chemical and structural validity, including the removal of free solvent molecules, addition of hydrogen atoms, resolution of disorders, and correction of potential structural inconsistencies. Density functional theory (DFT) calculations were performed to geometry optimize this whole set of curated structures. The Vienna Ab initio Simulation Package (VASP)[52] was employed with the Perdew−Burke−Ernzerhof (PBE) exchange-correlation functional,[53] D3/Becke-Johnson dispersion corrections,[54,55] and projector-augmented wave (PAW) pseudopotentials.[56] Their geometry optimizations were carried out using the conjugate gradient algorithm with an energy cutoff of 600 eV. Both atomic positions and lattice parameters were relaxed using an energy convergence criterion of 10^{-6} eV for the self-consistent field cycles and a force convergence threshold of 0.01 eV/Å for geometry optimization. For all cases, the Brillouin zone was sampled using a Monkhorst−Pack k-point mesh.[57] Some of these selected MOFs were further systematically modified via linker functionalization or linker substitution strategies. A few of these MOF variants have already been synthesized, while others are hypothetical. These modified MOFs were geometry optimized using the same DFT protocol described above. In total, 35 MOFs, comprising both pristine structures and their variants, were investigated in this

https://doi.org/10.1021/acs.chemmater.5c03403
Chem. Mater. 2026, 38, 5438−5452

study. For all materials, key textural properties, including the largest cavity diameter (LCD), pore limiting diameter (PLD), free pore volume, and void fraction, were calculated using the Zeo++ package.[58] A summary of all MOFs considered, along with their computed structural and textural properties, is provided in Table S1. The crystallographic information files (CIFs) of all optimized structures are shared on GitHub.[59]

2.2. Adsorption Simulations

Single-component CH_4 and H_2 adsorption isotherms, as well as those of their binary mixtures, were calculated for all MOFs at 298 K and total pressures up to 40 bar using GCMC simulations. For mixture adsorption, two compositions were considered: (i) 90:10 CH_4/H_2, and (ii) 25:75 CH_4/H_2. Both CH_4 and H_2 molecules were represented by single-site, uncharged Lennard-Jones (LJ) models, using TraPPE-united atom (TraPPE-UA)[60] and Buch[61] force fields, respectively. Buch force field for H_2 is known for its superior accuracy in reproducing experimental densities, solubilities, and diffusivities across a wide range of temperatures and pressures.[62] The role of quantum effects on H_2 adsorption was also evaluated by comparing the Buch model with an alternative single-site potential incorporating explicit quantum corrections,[63,64] as further discussed in Section 3.1.

The MOFs were treated as rigid frameworks, and LJ potential parameters for each MOF atom were taken from the Universal Force Field (UFF).[65] A 14 Å cutoff was applied for the van der Waals host/guest interactions, and LJ cross-interaction parameters were computed using Lorentz−Berthelot mixing rules. MOF unit cells were replicated in all three directions to construct supercells with each dimension longer than twice the selected cutoff distance. Specific adjustments of the force field parameters for the MOF atoms were applied as described in Section 3.1. The corresponding force field parameters for both MOF atoms and adsorbates are listed in Table S2. No electrostatic interactions were included since the models used to describe both adsorbates are uncharged. All adsorption simulations were performed using the Complex Adsorption and Diffusion Simulation Suite (CADSS) code.[66] For each isotherm point, 2×10^7 Monte Carlo cycles were used for both equilibration and production phases. Additionally, the adsorption enthalpy at zero coverage (ΔH_0) was calculated for CH_4 and H_2 in all MOFs using the revised Widom test particle insertion method.[67]

To rank the MOFs, we calculated the following metrics from the simulation results:

(i) Ideal selectivity (S^{ideal}), defined as the ratio of CH_4 ($Q_{CH_4}^{single}$) and H_2 ($Q_{H_2}^{single}$) uptakes at 298 K and 30 bar calculated from single-component GCMC simulations.

$$S^{ideal} = \frac{Q_{CH_4}^{single}[298\ K;\ 30\ bar]}{Q_{H_2}^{single}[298\ K;\ 30\ bar]} \quad (1)$$

(ii) Mixture selectivity ($S^{mixture}$), defined as the ratio of CH_4 ($Q_{CH_4}^{mixture}$)and H_2 ($Q_{H_2}^{mixture}$) uptakes at 298 K and 30 bar calculated from mixture GCMC simulations, normalized by the ratio of their mole fractions (y) in the bulk gas mixture phase.

$$S^{mixture} = \frac{Q_{CH_4}^{mixture}[298\ K;\ 30\ bar]/Q_{H_2}^{mixture}[298\ K;\ 30\ bar]}{y_{CH_4}/y_{H_2}} \quad (2)$$

(iii) CH_4 binary mixture sorption uptake ($Q_{CH_4}^{mixture}$) calculated from mixture GCMC simulations at 298 K and 30 bar.

(iv) CH_4 binary mixture working capacity (β) defined as the difference in CH_4 binary mixture sorption uptake calculated from mixture GCMC simulations at 30 and 1 bar, representative of typical PSA operating conditions.

$$\beta = Q_{CH_4}^{mixture}[298\ K;\ 30\ bar] - Q_{CH_4}^{mixture}[298\ K;\ 1\ bar] \quad (3)$$

(v) Adsorbent performance metric P as a proxy for process-level performance, which captures the trade-off between selectivity and working capacity.

$$P = \beta \times \ln(S^{mixture}) \quad (4)$$

GCMC simulations of $CH_4/H_2/H_2O$ ternary mixtures at 5% relative humidity were performed for selected high-performance MOFs to evaluate the impact of moisture in the feed stream. Both 90:10 and 25:75 CH_4/H_2 compositions on a dry basis were considered over a total pressure range of 1−30 bar. Water molecules were described using the TIP4P-Ew model,[68] and long-range electrostatic interactions were treated using the Ewald summation method.[69]

For comparing MOFs with commercial adsorbents, we evaluated the CH_4/H_2 separation performance of the widely used Zeolite 13X. The faujasite (FAU) zeolite topology[70] was modeled with a Si/Al ratio of 1.087, corresponding to 100 Si and 92 Al atoms at the T sites and in compliance with Löwenstein's rule. The Na^+ ion distribution was adopted from previous studies and kept fixed during simulations, as neither CH_4 nor H_2, given their weak interactions with the pore surface, are likely to displace the extra-framework cations.[71,72] GCMC simulations were performed for both single-component and binary mixtures under the same conditions used for the MOFs, using the CH_4 and H_2 models described above. For the H_2-zeolite interactions, LJ parameters for O and Na atoms were taken from Wender et al.,[73] while CH_4-zeolite interactions were defined by specific O−CH_4 and Na−CH_4 parameters proposed by Martin-Calvo and coworkers.[74] Si and Al atoms were treated as noninteracting species. Lorentz−Berthelot mixing rules were equally applied for cross-interactions where required. All parameter values are summarized in Table S2. The choice of these force fields was validated by a good agreement between experimental and simulated single-component adsorption isotherms,[75,76] as discussed in Section 3.1.

2.3. Molecular Dynamics Simulations

MD simulations were performed for CH_4 in a subset of MOFs showing high CH_4/H_2 selectivity and/or large CH_4 working capacity. The same molecular models and LJ parameters used in the GCMC simulations were employed for consistency. MOFs were treated as fully flexible, with intraframework interactions (bond stretching, angle bending, dihedral torsions, and improper rotations) equally described using UFF.[65] To better reflect the DFT-optimized geometries, equilibrium bond lengths in the harmonic bond potentials were adjusted to match the actual bond distances from the optimized structures. Although electrostatic interactions between MOF atoms are expected to play a minimal role in the flexibility of the structure, partial atomic charges were nevertheless assigned to the atoms of the MOFs using the MEPO-ML model.[77] All MD

https://doi.org/10.1021/acs.chemmater.5c03403
Chem. Mater. 2026, 38, 5438−5452

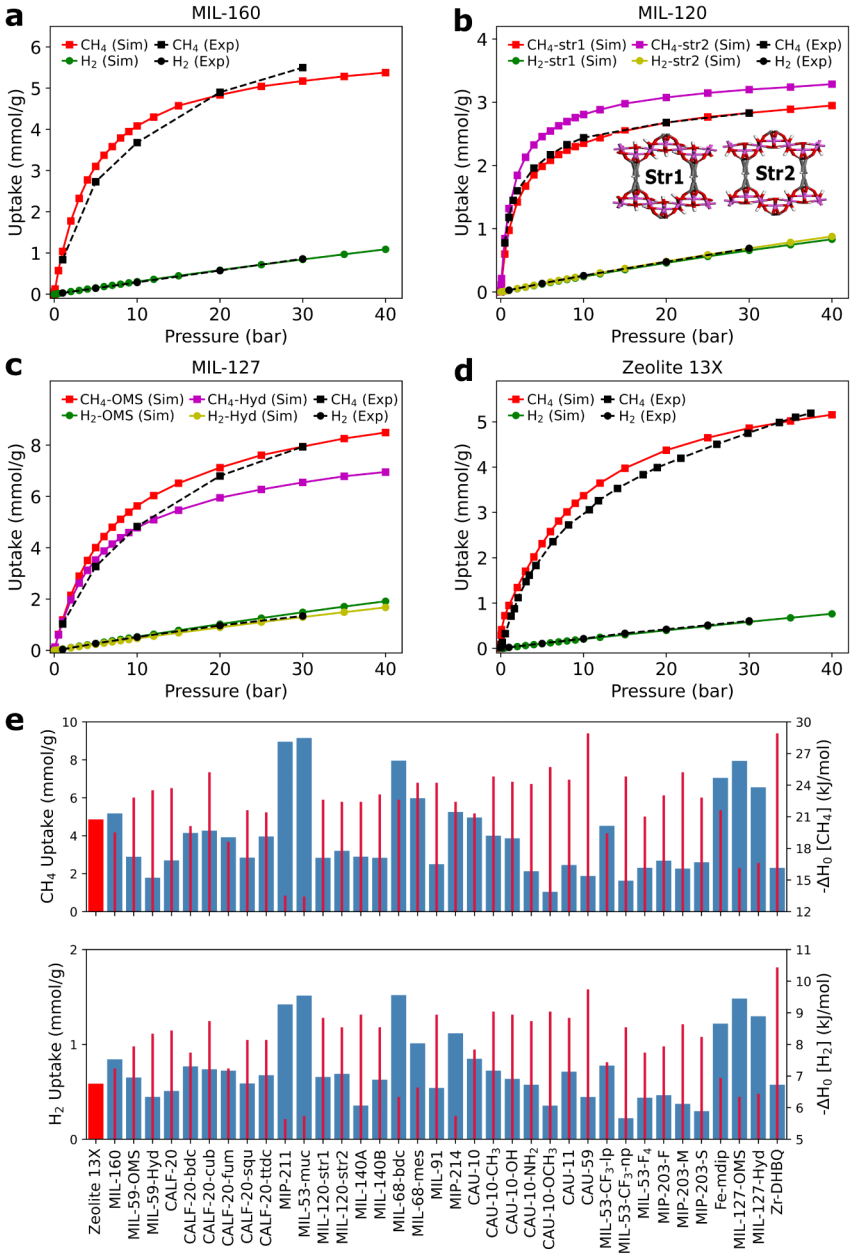

Figure 1. Simulated CH_4 and H_2 adsorption isotherms at 298 K, together with the corresponding experimental data, for (a) MIL-160(Al), (b) MIL-120(Al), and (c) MIL-127(Fe). MIL-120 exhibits two structural variants (Str-1 and Str-2) depending on the orientation of the μ_2−OH group (illustrated in the inset), while MIL-127 is modeled either with open metal sites (OMS) or in a hydrated (Hyd) form. (d) Simulated and experimental CH_4 and H_2 adsorption isotherms for Zeolite 13X. (e) Simulated CH_4 and H_2 uptakes at 298 K and 30 bar (blue bars for MOFs and red bar for Zeolite 13X) along with corresponding ΔH_0 (red lines) across all MOFs and Zeolite 13X. For comparison, experimental data for Zeolite 13X were taken from the literature.[75,76]

simulations were performed in the canonical (NVT) ensemble at 298 K using the Nosé-Hoover thermostat.[78,79] For each MOF, simulations employed the same supercells as in the GCMC calculations, covering CH_4 loadings from low coverage to saturation. The initial CH_4 distributions in the MOF pores were generated by canonical MC simulations. For each MOF-loading combination, a 2 ns equilibration phase was followed by a 20 ns production run. The MD simulations were carried out using the LAMMPS package.[80] Mean square displacement (MSD) profiles of CH_4 molecules were computed from the trajectories by averaging over multiple time origins for improved statistical accuracy. Self-diffusivities were extracted from the linear regime of the MSD curves using the Einstein relation. To ensure robustness, four independent initial CH_4 configurations were considered for all MOFs.

2.4. Single-Component Sorption Isotherms and Breakthrough Experiments

Single-component CH_4 and H_2 adsorption isotherms of MIL-160(Al), MIL-120(Al), and MIL-127(Fe) (MIL: Materials Institute Lavoisier) were measured at 298 K and pressures of 1−30 bar using a chromatographic method based on dynamic fixed-bed breakthrough experiments. These MOFs were synthesized according to previously reported protocols.[26,50,81] The synthesis procedures are described in Section S3 and the corresponding characterization results (Figures S1−S3) fit well

https://doi.org/10.1021/acs.chemmater.5c03403
Chem. Mater. 2026, 38, 5438−5452

with previous reports. The breakthrough experimental setup consists of three main sections: (1) gas preparation, (2) adsorption/desorption cycling, and (3) analysis. In the gas preparation section, N_2 carrier gas and the adsorbates were regulated by mass flow controllers, with system pressure maintained by back-pressure regulators. The adsorption/desorption section comprises a stainless-steel column placed in a temperature-controlled water bath and packed with the adsorbents initially saturated with H_2. A preprogrammed four-port valve alternated between pure CH_4 and H_2 streams until steady-state conditions were achieved. The effluent gas was directed to the analytical section, where a gas chromatograph equipped with a capillary column and a thermal conductivity detector (TCD) measured the outlet composition. Binary CH_4/H_2 breakthrough experiments were performed using the same setup, with the gas mixture prepared in the gas preparation section. Section S4 in the Supporting Information provides additional details on the experimental setup (Figure S4), procedure, and operating conditions (Tables S3−S5).

3. RESULTS AND DISCUSSION

3.1. CH_4 and H_2 Single-Component Adsorption

Single-component CH_4 and H_2 adsorption isotherms on MIL-160(Al), MIL-120(Al), and MIL-127(Fe) were determined from breakthrough experiments and used for benchmarking our GCMC strategy. The Al 2,5-furan dicarboxylate MOF MIL-160(Al) was selected as a benchmark MOF for this study due to its favorable combination of practical and structural attributes: a suitable 1D channel system with a moderate pore size (5.5 Å) for methane confinement, low-cost metal and linker components, high potential for green synthesis, ease of shaping, demonstrated mechanical stability, and scalability for industrial applications.[82,83] A modified version of UFF, with the interactions between the Al atoms and H atoms of the μ_2−OH groups of MIL-160(Al) with the adsorbate species turned off, provided a better agreement between the GCMC simulated and experimental CH_4 adsorption isotherms at 298 K, as shown in Figure S5. Using this force field for the MOF, we assessed the role of quantum effects in H_2 adsorption by comparing the Buch model with another commonly used potential[63,64] with Feynman-Hibbs correction.[84] The H_2 adsorption isotherms reported in Figure S6 indicate that quantum effects have a negligible influence on H_2 adsorption at room temperature. Figure 1a illustrates the resulting very good agreement between experimental and simulated CH_4 and H_2 adsorption isotherms for MIL-160(Al).

To further validate the simulation approach, including the selection of the refined force field parameters benchmarked on MIL-160(Al), experimental and predicted CH_4 and H_2 adsorption isotherms were compared for MIL-120(Al), another 1D channel-based Al carboxylate MOF with smaller pores, and MIL-127(Fe), a structurally and chemically distinct Fe oxocluster tetracarboxylate MOF with a 3D bimodal microporous system. As shown in Figure 1b and c, the simulated adsorption isotherms are in good agreement with the experimental data for both MOFs. Representative breakthrough curves at 298 K and 10 bar for the three MOFs are shown in Figure S7. For MIL-120(Al), previous DFT calculations identified two stable structure variants, referred to as Str-1 and Str-2 (inset of Figure 1b), distinguished by the orientation of their μ_2−OH groups pointing toward the pore.[26] Among the two, MIL-120(Al)-Str1 enabled to obtain a very good agreement between CH_4 experimental and simulated adsorption isotherms, whereas MIL-120(Al)-Str2 exhibits a higher CH_4 affinity and larger sorption uptake due to its symmetric μ_2−OH groups that enhance CH_4-framework interactions. MIL-127(Fe), which features a trinuclear Fe node with one Fe atom bounded to −OH group while the two others are coordinated to water molecules in its hydrated form (labeled as MIL-127-Hyd) or unsaturated in its activated form (labeled as MIL-127-OMS, with OMS for open metal sites). The CH_4 experimental adsorption isotherm closely matches the shape and high-pressure uptake of MIL-127-OMS, indicating that the structure with OMS better represents the experimental conditions. Although generic force fields like UFF are known to be unsatisfactory for capturing host/guest interactions in MOFs with OMS,[85] especially at very low pressure, we observe a rather good qualitative agreement in the working pressure range from 1 to 30 bar. Hence, in the context of systematic screening, we excluded the development of specific force fields for this MOF with OMS.

This validated computational approach was then applied to predict the CH_4 and H_2 single-component adsorption isotherms across the full set of MOFs investigated in this study, encompassing a broad range of pore sizes, shapes, and chemical environments. The MOF MIL-53(Al)-CF_3 is known to exhibit a stimulus-induced breathing behavior associated with a structural switching between large-pore (lp) and narrow-pore (np) forms.[86] Accordingly, both forms were considered to assess the impact of framework flexibility on single-component and binary mixture adsorption properties. A few pristine MOFs were systematically tuned via linker substitution and/or functionalization to modulate their adsorption properties. For instance, five isoreticular variants of the ultramicroporous Zn oxalate triazolate CALF-20(Zn)[25] (CALF: Calgary Framework) were considered from our previous work by replacing the oxalate linker with benzene-1,4-dicarboxylate (bdc), cubane-1,4-dicarboxylate (cub), fumarate (fum), squarate (squ), and thieno[3,2-*b*]thiophene-2,5-dicarboxylate (ttdc).[87] Similarly, in CAU-10(Al) (CAU: Christian Albrecht University), the 5-position of the benzene-1,3-dicarboxylate linker was functionalized with $-CH_3$, −OH, $-NH_2$, and $-OCH_3$ groups.[88] Other isoreticular systems studied include the large pore Al dicarboxylates MIL-68(Al)-bdc[89] and MIL-68(Al)-mes[90] (mes: mesaconate), and the ultramicroporous MIP-203(Zr) series (F, M, and S variants)[91] (MIP: Institute of Porous Materials of Paris). Among all MOFs explored in this study, only the five CALF-20(Zn) derivatives are hypothetical, while the remaining structures have been previously synthesized and reported in the literature. Figure S8 shows the single-component adsorption isotherms for four representative MOFs: those with largest and smallest LCDs (MIP-214(Fe)[28] and MIL-140A(Zr)[92]) and highest and lowest CH_4 uptakes at 30 bar (MIL-53(Al)-muc[93] and CAU-10(Al)-OCH_3[88]) while the others can be found on GitHub.[59]

To rank MOFs against commercial sorbents, we equally evaluated CH_4 and H_2 single-component adsorption isotherms for the conventional adsorbent Zeolite 13X. Figure 1d shows that the GCMC simulated adsorption isotherms for Zeolite 13X are in good agreement with the corresponding experimental data reported in the literature for both CH_4 and H_2.[75,76] Figure 1e further compares the CH_4 and H_2 uptakes at 298 K and 30 bar, together with their ΔH_0, across all investigated MOFs and Zeolite 13X. These predictions

https://doi.org/10.1021/acs.chemmater.5c03403
Chem. Mater. 2026, 38, 5438−5452

Table 1. Comparison of Experimental and Simulated CH_4/H_2 Mixture Selectivities at 30 Bar and CH_4 Working Capacities (1−30 Bar) for MIL-160(Al), MIL-120(Al), and MIL-127(Fe) at 90:10 and 25:75 CH_4/H_2 Compositions

	Experiment				Simulation			
	Selectivity [30 bar]		Working Capacity [1−30 bar](mmol/g)		Selectivity [30 bar]		Working Capacity [1−30 bar](mmol/g)	
MOF	90:10	25:75	90:10	25:75	90:10	25:75	90:10	25:75
MIL-160	29.0	35.6	4.07	2.93	29.3	37.2	4.12	3.20
MIL-120-str1	20.8	31.0	1.6	1.6	21.4	33.8	1.88	1.78
MIL-120-str2					39.7	57.5	1.93	2.10
MIL-127-OMS	16.8	21.3	5.96	3.58	17.2	21.8	6.62	4.32
MIL-127-Hyd					16.4	22.6	5.3	3.7

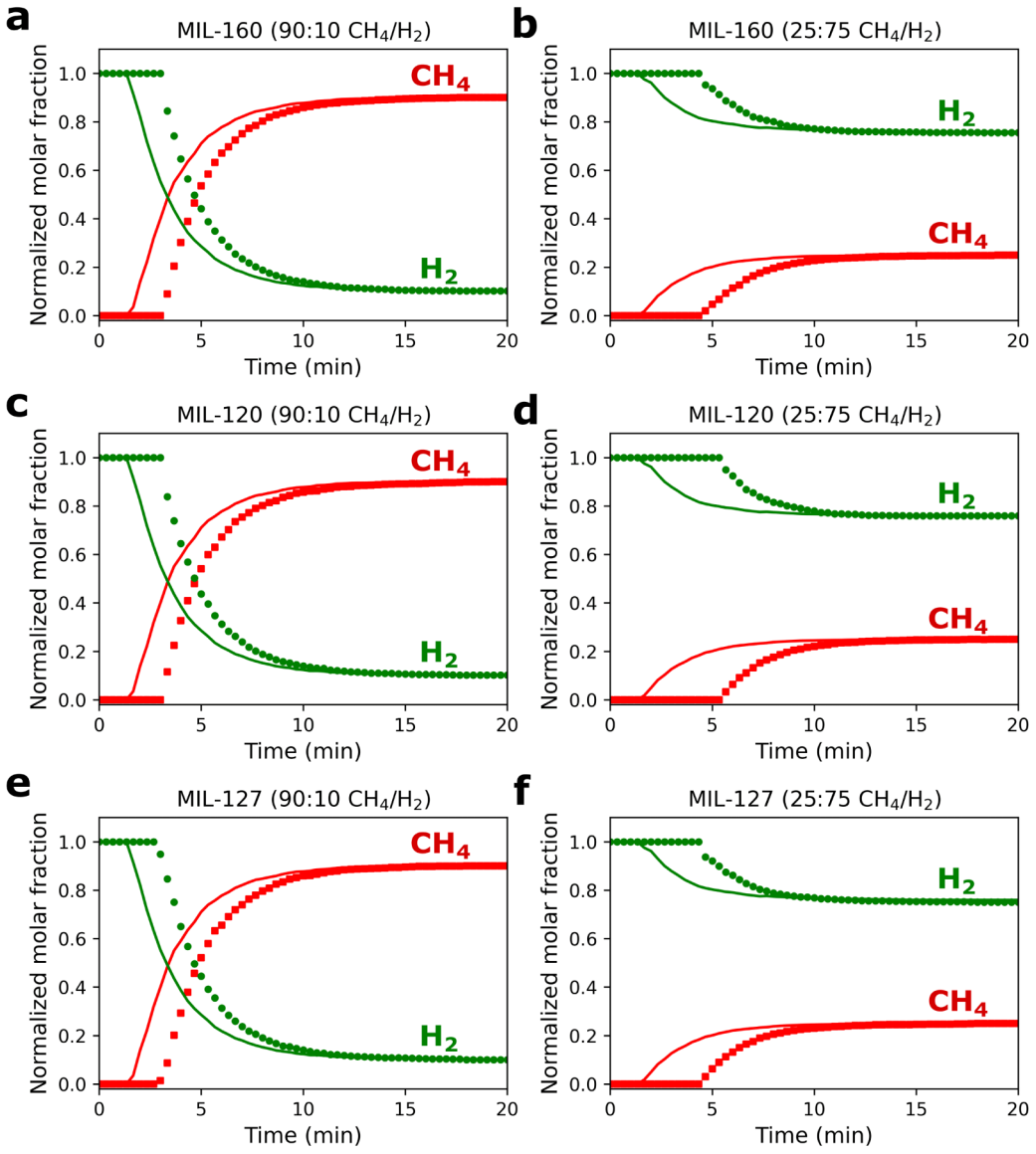

Figure 2. Binary CH_4/H_2 breakthrough curves at 298 K for (a) MIL-160(Al) with 90:10 CH_4/H_2, (b) MIL-160(Al) with 25:75 CH_4/H_2, (c) MIL-120(Al) with 90:10 CH_4/H_2, (d) MIL-120(Al) with 25:75 CH_4/H_2, (e) MIL-127(Fe) with 90:10 CH_4/H_2, and (f) MIL-127(Fe) with 25:75 CH_4/H_2 feed compositions. Continuous lines represent blank runs, while symbols correspond to experimental data.

revealed that several MOFs surpass the zeolite in terms of CH_4 uptake at 30 bar. Large-pore MOFs such as MIL-53(Al)-muc[93] (muc: muconate), MIP-211(Al),[93] MIL-68(Al)-bdc,[89] MIL-127(Fe),[50] and the Fe oxocluster pyrazole carboxylate MIP-214(Fe)[28] exhibit particularly large CH_4 uptake, exceeding 6 mmol/g at 30 bar. In contrast, H_2 uptake remains low across all materials, below 1.5 mmol/g at 30 bar, highlighting the inherently weak interactions between H_2 molecules and the MOF frameworks. The computed ΔH_0 values show that CH_4 exhibits moderate to strong interactions (ΔH_0 = −13.3 to −28.8 kJ/mol), whereas H_2 interactions are considerably weaker (ΔH_0 = −5.6 to −10.4 kJ/mol). This distinct

https://doi.org/10.1021/acs.chemmater.5c03403
Chem. Mater. 2026, 38, 5438−5452

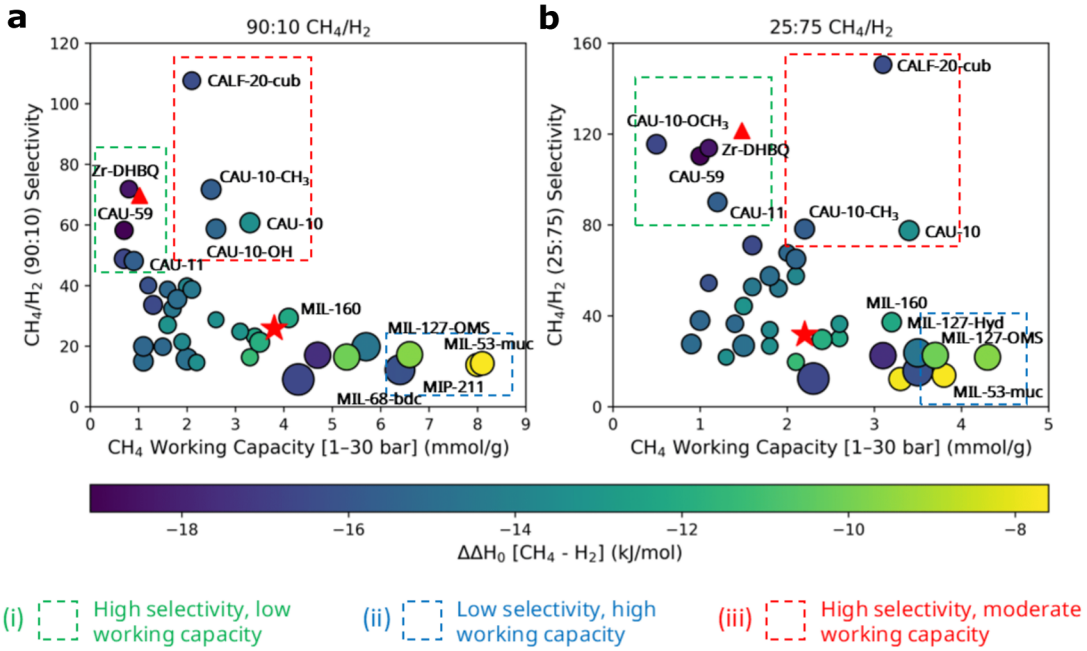

Figure 3. Comparison of MOF performance in terms of CH_4 working capacity (1−30 bar) and CH_4/H_2 selectivity at 30 bar and 298 K for (a) 90:10 CH_4/H_2 mixture and (b) 25:75 CH_4/H_2 mixture. Data points are color-coded based on $\Delta\Delta H_0$ ($\Delta\Delta H_0 = \Delta H_0$ (CH_4) − ΔH_0 (H_2)) and circle sizes are scaled according to the LCD of each MOF. Zeolite 13X is included as a benchmark, represented by a red star. The red triangle represents NELVAC, a MOF recently identified as the most promising adsorbent through a machine learning-based screening study.[42] Three distinct classes of promising materials are highlighted: (i) MOFs exhibiting high CH_4/H_2 selectivity but low working capacity, (ii) MOFs with low selectivity but high working capacity, and (iii) MOFs with high selectivity and moderate working capacity.

adsorption behavior between CH_4 and H_2, both in terms of uptake and enthalpy, indicates that an effective thermodynamics-driven separation is achievable under equilibrium conditions using MOFs. As a further step, we calculated the CH_4/H_2 ideal selectivities at 298 K and 30 bar across all MOFs from their single-component adsorption isotherms, providing a baseline for performance comparison. The selectivity values range from 2.9 for CAU-10(Al)-OCH_3 to 8.8 for MIP-203(Zr)-S, confirming the preferential uptake of CH_4 over H_2 in all cases. The predicted ideal selectivities show good agreement with the experimental values for the three MOFs extracted from the experimental single-component adsorption isotherms. Specifically, the predicted and experimental ideal selectivities are 6.1 vs 6.4 for MIL-160(Al); 4.3 (Str1) and 4.6 (Str2) vs with 4.1 for MIL-120(Al); and 5.3 (MIL-127(Fe)-OMS) and 5.0 (MIL-127(Fe)-Hyd) vs 5.9 for MIL-127(Fe).

3.2. CH_4/H_2 Binary Mixture Adsorption

Ideal selectivity is widely used in high-throughput computational screening to rank MOF separation performance; however, this metric overlooks competitive coadsorption effects that take place under realistic mixture conditions, which can substantially misrepresent the true selectivity of a material. In this context, binary mixture GCMC simulations were performed for the three benchmark MOFs, i.e., MIL-160(Al), MIL-120(Al), and MIL-127(Fe) at 298 K and two scenarios: (i) 90:10 CH_4/H_2 binary composition relevant to H_2 recovery from natural gas grids, and (ii) 25:75 CH_4/H_2, representative of H_2 purification following SMR. The simulated CH_4/H_2 mixture selectivity alongside CH_4 working capacity (1−30 bar) for these MOFs are summarized in Table 1. Importantly, the resulting mixture selectivity values are generally significantly higher than the corresponding ideal selectivities discussed above. For comparison, binary CH_4/H_2 breakthrough experiments were performed for the same three MOFs at 298 K under 1 and 30 bar for the two feed compositions. The corresponding breakthrough curves at 30 bar are shown in Figure 2, with those at 1 bar are presented in Figure S9. The binary breakthrough profiles, compared with blank runs, display a single mass-transfer zone approaching the feed composition, characteristic of binary systems with two adsorbing species and forming the basis of the chromatographic determination of binary equilibrium loadings.[94] Indeed, Table 1 shows that experimental CH_4/H_2 mixture selectivity and CH_4 working capacity compare very well with the simulated data calculated at the same conditions for the three MOFs, while the calculated ideal selectivity substantially underestimates the performance. This observation highlights that a correct performance evaluation of MOFs for CH_4/H_2 separation critically requires real gas binary mixture simulations. This overall methodology was subsequently extended to the broader set of MOFs to predict their CH_4/H_2 separation performance. The simulated mixture adsorption isotherms (Figure S10) highlight negligible H_2 uptake even at high pressures for all MOFs, reflecting the stronger enthalpic affinity of CH_4 and its preferential occupation of adsorption sites, as well as its larger molecular size and bulky spherical shape, that contribute to sterically limit the adsorption of H_2 in the MOF pores. Figure S11 compares ideal selectivity with mixture selectivity at 30 bar for 90:10 and 25:75 CH_4/H_2 mixtures across all MOFs. Consistent with the three benchmark materials validated experimentally, ideal selectivity significantly underestimates the actual separation performance under mixture conditions.

Figure 3a and b illustrates the separation performance of all MOFs with the plot of CH_4/H_2 selectivity for the 90:10 and 25:75 binary mixtures at 30 bar alongside its CH_4 working

https://doi.org/10.1021/acs.chemmater.5c03403
Chem. Mater. 2026, 38, 5438−5452

capacity between 30 and 1 bar. Marker size represents the LCD, and color indicates the difference between the zero-coverage adsorption enthalpies of CH_4 and H_2 ($\Delta\Delta H_0$). Similar comparison plots for the two mixtures with CH_4 uptake at 30 bar instead of CH_4 working capacity are shown in Figure S12. Figure S13 illustrates the pressure dependence of the simulated CH_4/H_2 selectivity for a set of representative MOFs, indicating that the selectivity remains largely invariant across the 1−30 bar range relevant to PSA operation. The comparison plots reveal three classes of promising MOF materials with (i) high selectivity and low working capacity, including CAU-11(Al),[95] CAU-59(Ce),[96] and Zr-DHBQ[97] (DHBQ: 2,5-dihydroxy-1,4-benzoquinone); (ii) low selectivity and high working capacity, comprising MIL-53(Al)-muc, MIP-211(Al), MIL-127(Fe)-OMS, and MIL-68(Al)-bdc; and (iii) a balanced performance in terms of selectivity and working capacity, featuring CAU-10(Al), CAU-10(Al)-CH_3, and CAU-10(Al)-OH, along with the modulated CALF-20(Zn)-cub. The relative MOF ranking is globally consistent between the 90:10 CH_4/H_2 and 25:75 CH_4/H_2 mixtures, with some notable variations. For instance, MIL-53(Al)-muc and MIP-211(Al) show ∼1.5 mmol/g higher CH_4 working capacity than MIL-127(Fe)-OMS at 90:10, whereas MIL-127(Fe)-OMS outperforms them at 25:75, with 0.6−1.0 mmol/g higher working capacity. Interestingly, MOFs with lower CH_4 capacities but higher ΔH_0, such as CAU-11(Al) and Zr-DHBQ, exhibit improved performance at 25:75 composition, achieving simultaneous gains in selectivity and capacity. A similar trend is observed for CALF-20(Zn)-cub.

The selectivity-working capacity trade-off evident from Figure 3a and b is more pronounced for the 90:10 CH_4/H_2 mixture, where CH_4 is the predominant component that is preferentially adsorbed. Optimizing both selectivity and working capacity simultaneously is challenging. MOFs with small pores (high degree of confinement) provide stronger CH_4-framework interactions and thus higher CH_4/H_2 selectivity, but their limited pore volume restricts CH_4 uptake. Conversely, larger-pore MOFs allow higher CH_4 loading and working capacity due to greater accessible volume, yet weaker confinement lowers the $\Delta\Delta H_0$, reducing CH_4/H_2 selectivity. This inverse relationship highlights a fundamental design trade-off requiring precise tuning of pore size and chemistry. The trade-off is less pronounced for the 25:75 CH_4/H_2 mixture, where CH_4 is the minority component. As shown in Figure S14, selectivities are generally higher at this composition, except for MIL-53(Al)-muc and MIP-211(Al), which exhibit small $\Delta\Delta H_0$. In most MOFs, CH_4 adsorption remains favored, and its preferential adsorption at lower partial pressures, combined with pore-blocking effects, suppresses H_2 uptake. The trend in CH_4 working capacity is more complex. While CH_4 uptake and working capacity are typically higher for the 90:10 mixture, some MOFs with strong CH_4-framework interactions show slightly lower capacities due to the early saturation of the adsorption site, which decreases the uptake difference between adsorption and desorption pressures.

Among the evaluated materials, CAU-10(Al) and its functionalized derivatives, CAU-10(Al)-CH_3 and CAU-10(Al)-OH, exhibit an excellent balance between CH_4/H_2 selectivity and CH_4 working capacity. These Al-based MOFs have one-dimensional channels that provide strong thermodynamic preference for CH_4 while maintaining moderate pore volumes for appreciable uptake. Linker functionalization enhances molecular confinement and adjusts the chemical environment of the pore, though often at the expense of accessible volume. A comparative analysis of the CAU-10(Al) series for both feed compositions is shown in Figure S15a and b. Similarly, we investigated linker substitution in CALF-20(Zn) to tune its separation performance. These hypothetical CALF-20(Zn) derivatives exhibit increased CH_4 uptake and working capacity as compared to pristine CALF-20(Zn). In particular, CALF-20(Zn)-cub uniquely combines higher confinement for CH_4 and larger CH_4 uptake as shown in Figure S15c and d. We also analyzed the impact of framework flexibility in MIL-53(Al)-CF_3 on separation performance. The lp phase exhibits higher CH_4 working capacities (3.5 and 2.4 mmol/g for 90:10 and 25:75 CH_4/H_2 mixtures) than the np phase (1.2 and 1.1 mmol/g), due to its larger pore size. However, the np phase shows higher CH_4/H_2 mixture selectivities for the two binary mixtures (40 and 54) compared to the lp phase (21 and 30) due to increased confinement. We further compared the separation performance of these investigated MOFs against Zeolite 13X, denoted by a red star in Figure 3a and b. Zeolite 13X is shown to exhibit a reasonable balance between selectivity and working capacity; however, the benchmark MOF in this study, MIL-160(Al), marginally outperforms this zeolite in both metrics. Moreover, several MOFs evaluated here exhibit even higher selectivity and larger working capacity than Zeolite 13X, highlighting their potential for CH_4/H_2 separation. As a final comparison, we assessed NELVAC (a zinc diphosphonate material),[98] a MOF predicted as a promising CH_4/H_2 selective sorbent in a recent machine learning-assisted high-throughput computational screening based on single-component adsorption and ideal selectivity evaluation.[42] Using the same simulation conditions and protocols adopted in this work, GCMC simulations were carried out to evaluate the separation performance of this MOF using binary mixture. We obtained selectivities of 70 and 120 for the 90:10 and 25:75 mixtures, respectively, with corresponding CH_4 working capacities of 1.0 mmol/g and 1.5 mmol/g, as denoted by the red squares in Figure 3a and b. This places this material in the category of materials with high selectivity but low CH_4 working capacity. Moreover, this MOF contains unreacted 2-methylpiperazine in its pore, that cannot be removed without framework collapse making this material unsuitable as an adsorbent.

We further analyzed the separation mechanism of one representative MOF from each performance class: CAU-11(Al) (high selectivity, low working capacity), MIP-211(Al) (low selectivity, high working capacity), and CAU-10(Al) (balanced performance), along with the benchmark MIL-160(Al). GCMC simulations showed that CH_4 adsorption in these MOFs is mainly governed by pore geometry and weak dispersion forces, rather than strong binding to specific adsorption sites. MIL-160(Al) and CAU-10(Al) confines CH_4 near linker regions, CAU-11(Al) promotes packing within its symmetric channel, and MIP-211(Al) displays uniform adsorption across its large pore. These results emphasize the dominant influence of pore architecture on CH_4 uptake. In contrast, H_2 interacts only weakly with the MOF frameworks, leading to preferential CH_4 adsorption under binary mixture conditions. Further discussion of adsorption mechanisms is provided in Section S8 (Figures S16−S18).

https://doi.org/10.1021/acs.chemmater.5c03403
Chem. Mater. 2026, 38, 5438−5452

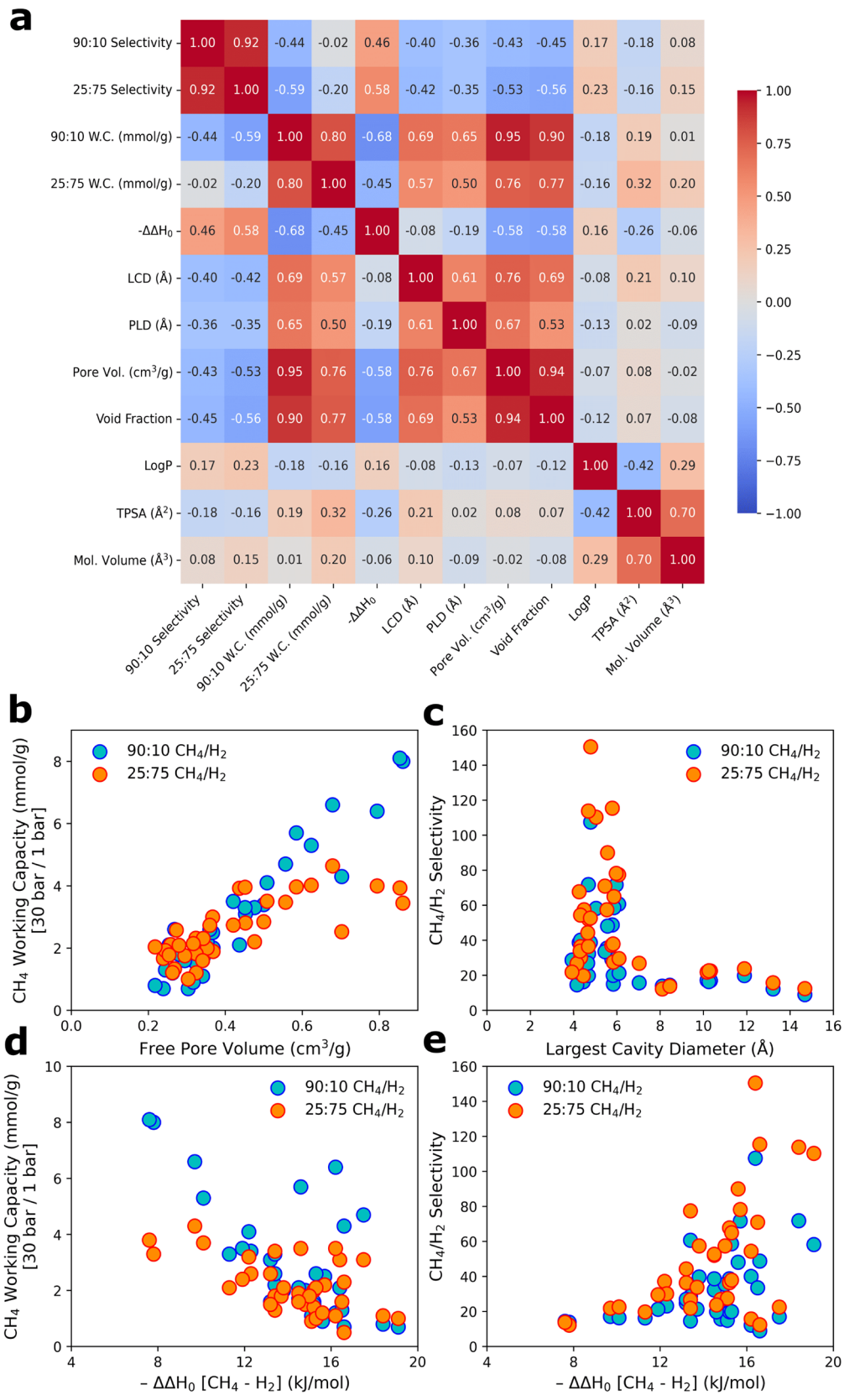

Figure 4. (a) Correlation matrix heatmap illustrating relationships among performance metrics, structural properties, and linker descriptors. Performance metrics include CH_4/H_2 selectivity and CH_4 working capacity for 90:10 and 25:75 feed mixtures, as well as $\Delta\Delta H_0$. Structural descriptors comprise LCD, PLD, free pore volume, and void fraction. Linker descriptors include LogP, TPSA, and molecular volume. Each cell reports the Pearson correlation coefficient between two variables, with shading indicating strength and direction of correlation. (b) CH_4 working capacity (1−30 bar) as a function of free pore volume. (c) CH_4/H_2 selectivity at 30 bar versus LCD. (d) CH_4 working capacity versus $\Delta\Delta H_0$. (e)

https://doi.org/10.1021/acs.chemmater.5c03403
Chem. Mater. 2026, 38, 5438−5452

Figure 4. continued

CH_4/H_2 selectivity versus $\Delta\Delta H_0$. Together, these plots highlight the role of pore geometry and adsorption energetics in governing CH_4/H_2 separation performance.

3.3. Structure–Performance Relationships

We further investigated how key MOF textural properties and linker characteristics influence the CH_4/H_2 separation behavior across the entire set of MOFs. The performance metrics include CH_4/H_2 selectivity and CH_4 working capacity for 90:10 and 25:75 CH_4/H_2 mixtures, and $\Delta\Delta H_0$, which captures the thermodynamics driving force for separation. These adsorption metrics were analyzed against four MOF geometric characteristics, i.e., LCD, PLD, free pore volume and void fraction. Additionally, three chemical descriptors of organic linkers were considered: partition coefficient (logP), total polarizable surface area (TPSA), and molecular volume, all computed using the RDKit package,[99] with the objective to account for linker hydrophobicity, polarizability, and size, respectively, features that can potentially impact the strength of the host/guest interactions and hence the resulting adsorption energetics. To establish structure–performance relationships, we computed Pearson's correlation coefficient (ρ) for each pair of properties and performance metrics. The resulting correlation matrix is shown in Figure 4a. A visual illustration of some key trends is presented in Figure 4b–e, which plots CH_4 working capacity between 30 and 1 bar against free pore volume, CH_4/H_2 selectivity against LCD, and both selectivity and working capacity against $\Delta\Delta H_0$. Several insights emerge from this analysis. First, CH_4 uptake and working capacity are strongly correlated with free pore volume, highlighting the dominant role of pore volume in determining gas loading under high-pressure conditions. This correlation is particularly high for the 90:10 CH_4/H_2 mixture (ρ = 0.95). A similar correlation is observed between working capacity and void fraction (ρ = 0.90 for 90:10, and ρ = 0.77 for 25:75) in line with the strong correlation between free pore volume and void fraction themselves (ρ = 0.94). In contrast, CH_4/H_2 selectivity shows an inverse trend with pore size. As LCD increases, selectivity generally decreases exponentially, suggesting that a higher degree of confinement enhances CH_4 selectivity by enhancing dispersive interactions and by excluding H_2 due to its smaller size and weaker interaction strength. This is further supported by the moderately negative correlation (ρ = −0.45 for 90:10, and ρ = −0.56 for 25:75) between selectivity and void fraction, reflecting the trade-off between working capacity and selectivity.

Additionally, an inverse correlation is observed between working capacity and $\Delta\Delta H_0$ (ρ = −0.68 for 90:10, and ρ = −0.45 for 25:75) and selectivity shows a roughly exponential increase with $\Delta\Delta H_0$. This observation confirms that strong host/guest interactions typically result from more confined environment and smaller pores, which, while enhancing selectivity, limit the overall pore volume available for gas adsorption. This interplay reinforces the trade-off between capacity and selectivity in MOF design and emphasizes the importance of balancing thermodynamic selectivity with accessible pore volume to optimize performance. Analysis of additional descriptors suggest that pore chemistry plays a less important role compared to the geometry as evident from the correlations from Figure 4a. Nevertheless, we observe that higher hydrophobicity (indicated by logP) and lower polarizability (TPSA) of linkers enhance selectivity, in line with the hydrophobic, nonpolar nature of CH_4. The molecular volume of linker units shows weak correlation with the performance metrics for the 25:75 mixture and negligible correlation for the 90:10 mixture.

3.4. CH_4 Diffusion in Representative MOFs

GCMC simulations identified several MOFs with promising thermodynamic CH_4/H_2 separation performance. However, in PSA processes, kinetics is equally critical as working capacity and selectivity. Gas transport within MOF pores may influence the rate of adsorption and ultimately governs the throughput and productivity of the overall process.[100] For industrial-scale PSA operations to be economically viable, gas diffusion must be sufficiently fast. We therefore computed the self-diffusivity of CH_4 at various loadings using equilibrium MD simulations for four representative materials, including MOFs from the three promising families, CAU-10(Al), CAU-11(Al), MIP-211(Al), and the benchmark MIL-160(Al). Given that H_2 adsorption is minimal under mixture conditions, CH_4 diffusivity is expected to be the primary factor influencing adsorption kinetics in these systems.

Figure 5 presents the self-diffusivities of CH_4 as a function of loading for the four MOFs. Across all MOFs and loadings, the

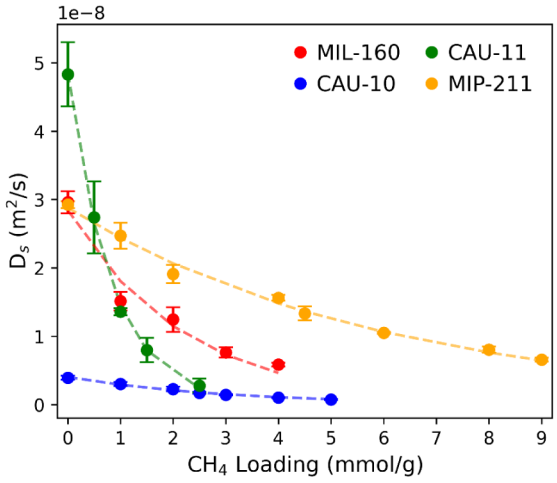

Figure 5. Self-diffusivity of CH_4 in MIL-160(Al), CAU-10(Al), CAU-11(Al), and MIP-211(Al) at 298 K as a function of CH_4 loading. Each point represents the mean of four independent simulation replicas, and error bars denote the corresponding standard deviation. The dashed lines are added as visual aids.

CH_4 self-diffusivities are found to be within the range 10^{-8} to 10^{-9} m^2/s. These values are well above the typical lower threshold of 10^{-11} m^2/s, which is generally considered as minimum diffusivity for enabling rapid cycles in PSA processes.[94] Therefore, these results suggest that CH_4 diffusion is sufficiently fast in all four MOFs for practical PSA operation. As expected, self-diffusivity decreases with increasing loading due to a reduced frequency of molecular hopping between adsorption sites and neighboring vacant sites. The progressive occupation of adsorption sites with higher loading imposes

https://doi.org/10.1021/acs.chemmater.5c03403
Chem. Mater. 2026, 38, 5438−5452

additional steric hindrance, further restricting molecular mobility.

Diffusion in porous materials arises from a complex interplay between pore geometry, adsorption strength, free energy barriers, and guest−guest interactions. In most cases, CH_4 is expected to diffuse faster in MOFs with larger pores and windows, slower in those with stronger host/guest interactions, and often faster in frameworks that exhibit structural flexibility. Adsorbate−adsorbate interactions, particularly at higher loadings, also influence the diffusion process by introducing additional crowding effects. Across the full loading range investigated, CH_4 diffusion is fastest in MIP-211(Al), which features large pore size (LCD = 8.1 Å) and weak CH_4 affinity (ΔH_0 = −13.4 kJ/mol). At higher loadings, MIL-160(Al) follows, benefiting from a relatively moderate CH_4 affinity (ΔH_0 = −19.4 kJ/mol). CAU-10(Al) exhibits the slowest diffusion among the four MOFs, which can be attributed to its pore window (PLD = 3.9 Å) being close to the kinetic diameter of CH_4, combined with its rather rigid-like framework. Interestingly, CAU-11(Al) demonstrates an unusual trend: despite having strong host/guest interactions for CH_4 (ΔH_0 = −24.4 kJ/mol) that contribute to slow down the diffusion of this species at higher loadings, this MOF shows the fastest diffusion at infinite dilution. This can likely be attributed to its relatively large pore window and potential framework flexibility, particularly due to its V-shaped linker, which results in low free energy barriers between adsorption sites. At low loadings, where adsorbate−adsorbate interactions are minimal, such geometric factors tend to dominate diffusion behavior. Together, these results highlight how CH_4 diffusivity in MOFs is governed by a balance between pore size, interaction strength, and framework dynamics. Because the selected four MOFs span a wide range of structural and chemical characteristics, the trends observed here provide qualitative insights that are broadly applicable to the wider set of materials studied in this work.

3.5. Practical Considerations for PSA

Our systematic computational evaluation shows that MOF selection should be guided by specific application requirements. MOFs with high selectivity but low working capacity are suited for high-purity applications where productivity is of lower importance, while those with low selectivity and high working capacity favor H_2 production with lower purity. Materials with balanced performance offer a practical compromise between purity and productivity. We further computed the adsorbent performance metric P as defined in eq 4, which serves as a proxy for cyclic PSA process efficiency by jointly accounting for selectivity and working capacity. Figure S19 presents the CH_4/H_2 selectivity versus CH_4 working capacity for both mixture compositions, with each material color-coded by its corresponding P value. We observe that MOFs with higher working capacity generally exhibit higher P values than those with high selectivity but lower working capacity, indicating that working capacity plays a dominant role in governing overall cyclic PSA performance. This metric provides an additional perspective by combining selectivity and working capacity, thereby serving as a useful proxy for process-level performance. Beyond adsorption performance, factors such as synthesis scalability, stability, and sustainability can outweigh marginal differences in selectivity or capacity. Among the evaluated materials, CAU-10(Al) emerges as a particularly promising MOF for CH_4/H_2 separation, which can be synthesized at the multikilogram scale under green, industrially feasible conditions while maintaining high crystallinity and porosity.[101] CAU-11(Al), with its intrinsic hydrophobicity, is especially attractive for humid gas streams, whereas MIP-211(Al), MIL-53(Al)-muc, and the experimentally validated MIL-127(Fe), featuring larger pore volumes, are well suited for high-productivity PSA operations. Table S6 summarizes the practical viability of these selected promising MOFs, alongside those experimentally synthesized in this work, in terms of synthesis conditions, stability, scalability, cost, and sustainability. In contrast to previous high-throughput computational screening studies that often propose MOFs with limited industrial relevance, our approach provides a diverse set of candidates with strong CH_4/H_2 separation performance under realistic conditions, complementary advantages and trade-offs, and high potential for practical deployment.

A few materials exhibit high CH_4 uptake at the desorption pressure of 1 bar, which can limit working capacity, as evident from comparing Figure 3 and Figure S12. For such cases, a vacuum pressure swing adsorption (VPSA) process operating at reduced desorption pressure may be employed to enhance working capacity and facilitate efficient adsorbent regeneration. For example, in several MOFs, including CAU-10(Al) (+1.6 mmol/g), CALF-20(Zn)-cub (+2.2 mmol/g), and CAU-11(Al) (+1.5 mmol/g), the CH_4 uptake at 30 bar exceeds the 1−30 bar working capacity for the 90:10 mixture by more than 1.5 mmol/g. These insights emphasize that optimal process design must balance material performance with operating conditions to maximize productivity and energy efficiency. Integrating such molecular-level understanding with process modeling will be essential for translating these findings into industrial practice.

Real industrial gas streams often contain additional components like CO_2, CO, N_2, and moisture, which can introduce competitive adsorption effects and influence CH_4/H_2 separation performance. In particular, CO_2 is expected to compete strongly with CH_4 due to its higher polarizability and quadrupole moment, while H_2O can significantly affect adsorption in hydrophilic frameworks by preferentially occupying strong binding sites. However, in practical scenarios, CO_2 is typically removed upstream, via amine scrubbing or PSA during natural gas upgrading prior to H_2 blending, and via PSA after the water−gas shift step in SMR processes. Similarly, dehydration units reduce moisture content to trace levels. Therefore, the binary CH_4/H_2 mixtures considered in this study represent a meaningful idealization of industrial conditions. Nevertheless, residual moisture may still impact separation performance. To assess the robustness of selected promising materials, we performed ternary $CH_4/H_2/H_2O$ GCMC simulations at 5% relative humidity for three representative MOFs: CAU-10(Al), CAU-11(Al), and MIP-211(Al). Table S7 compares CH_4 and H_2 uptakes under dry and humid conditions for both 90:10 and 25:75 CH_4/H_2 mixtures over the 1−30 bar pressure range, along with H_2O uptake. The results show negligible impact of moisture, with CH_4 and H_2 uptakes preserved, in line with rather hydrophobic behaviors of these MOFs as reported previously.[93,102,103]

4. CONCLUSIONS

In this study, we performed a systematic evaluation of MOFs for thermodynamics-driven CH_4/H_2 separation, targeting two key industrial scenarios: H_2 recovery from natural gas grids after cotransport with CH_4, and H_2 purification following

https://doi.org/10.1021/acs.chemmater.5c03403
Chem. Mater. 2026, 38, 5438−5452

SMR. Rather than relying on serendipitous experimental exploration or time-consuming high-throughput screening workflows with limited predictive accuracy, we adopted a focused and rigorous approach by performing detailed atomistic simulations under practically relevant conditions on a carefully selected set of viable MOFs considering ease of synthesis, cost-effectiveness of metal and linker components, structural and chemical stability, scalability, and sustainability. We first validated our simulation methodology against single-component adsorption isotherms on a few MOFs to ensure prediction accuracy. Subsequently, single-component and binary mixture GCMC simulations were used to assess the separation performance of a representative set of MOFs. Three promising classes of materials emerged: MOFs with (i) high CH_4/H_2 selectivity with low CH_4 working capacity, (ii) low CH_4/H_2 selectivity with high CH_4 working capacity, and (iii) a balanced profile of high CH_4/H_2 selectivity with moderate CH_4 working capacity. These findings highlight the intrinsic trade-off between selectivity and capacity but also identify several promising candidates tailored to different process requirements. Several MOFs were shown to outperform the commercial adsorbent Zeolite 13X. To better understand the separation process, we rationalized the performance of MOFs in terms of pore size, geometry, and chemical functionalities. Finally, MD simulations were performed to study CH_4 diffusion in a subset of promising MOFs, evaluating their potential for use in PSA applications. Building on the computational insights presented in this work, targeted mixture adsorption experiments using pilot-scale setups could serve as a critical next step toward the development of advanced gas separation systems based on high-performance MOF adsorbents.

■ ASSOCIATED CONTENT

Data Availability Statement

All simulations in this work were carried out using VASP, LAMMPS, and CADSS, which are widely used packages for molecular simulations. Data processing and visualization were performed with standard Python libraries. The MOF structures, along with the simulated single-component and mixture adsorption isotherms, are available on GitHub at https://github.com/prantardutta/MOF-Methane-Hydrogen.

Supporting Information

The Supporting Information is available free of charge at https://pubs.acs.org/doi/10.1021/acs.chemmater.5c03403.

List of investigated structures; force field parameters; MOF synthesis and characterization; experimental conditions of breakthrough studies; force field benchmarking; single-component adsorption; mixture separation; microscopic adsorption mechanisms; practical aspects of industrial separation (PDF)

■ AUTHOR INFORMATION

Corresponding Authors

Guillaume Maurin − *ICGM, Université de Montpellier, CNRS, ENSCM, Montpellier 34293, France; Institut Universitaire de France, France;* orcid.org/0000-0002-2096-0450; Email: guillaume.maurin1@umontpellier.fr

José A. C. Silva − *CIMO, LA SusTEC, Instituto Politécnico de Bragança, Campus de Santa Apolónia, Bragança 5300-253, Portugal;* orcid.org/0000-0003-1778-3833; Email: jsilva@ipb.pt

Authors

Prantar Dutta − *ICGM, Université de Montpellier, CNRS, ENSCM, Montpellier 34293, France; OneTech, R&D, CSTJF, TotalEnergies, Pau 64018, France*

Adriano Henrique − *CIMO, LA SusTEC, Instituto Politécnico de Bragança, Campus de Santa Apolónia, Bragança 5300-253, Portugal;* orcid.org/0000-0002-5227-9790

Writakshi Mandal − *Institut des Matériaux Poreux de Paris, ESPCI Paris, Ecole Normale Supérieure, CNRS, PSL University, Paris 75005, France*

Laura Bueno − *CIMO, LA SusTEC, Instituto Politécnico de Bragança, Campus de Santa Apolónia, Bragança 5300-253, Portugal;* orcid.org/0009-0004-1314-8853

Rosana V. Pinto − *Institut des Matériaux Poreux de Paris, ESPCI Paris, Ecole Normale Supérieure, CNRS, PSL University, Paris 75005, France*

Yann Magnin − *OneTech, R&D, CSTJF, TotalEnergies, Pau 64018, France*

Sandra Barbouteau − *OneTech, R&D, CSTJF, TotalEnergies, Pau 64018, France*

Georges Mouchaham − *Institut des Matériaux Poreux de Paris, ESPCI Paris, Ecole Normale Supérieure, CNRS, PSL University, Paris 75005, France;* orcid.org/0000-0001-8696-9733

Christian Serre − *Institut des Matériaux Poreux de Paris, ESPCI Paris, Ecole Normale Supérieure, CNRS, PSL University, Paris 75005, France;* orcid.org/0000-0003-3040-2564

Complete contact information is available at: https://pubs.acs.org/10.1021/acs.chemmater.5c03403

Author Contributions

Y.M., C.S., J.A.C.S., and G.Ma. conceived and designed the study. P.D. performed the computational simulations and data analysis. W.M. and R.V.P. synthesized the MOFs and performed the characterization studies. A.H. and L.B. performed the breakthrough experiments and data analysis. The computational work was supervised by Y.M. and G.Ma.; MOF synthesis and characterization were supervised by G.Mo. and C.S.; the breakthrough experiments were supervised by J.A.C.S., while S.B. was responsible for project administration and coordination. All authors contributed to the interpretation of the results and to the preparation of the manuscript.

Notes

The authors declare no competing financial interest.

■ ACKNOWLEDGMENTS

The authors thank TotalEnergies OneTech for financial support of this project. The computational work was performed using HPC resources from GENCI-CINES (Grant A0180907613). The experimental resources used in this work were also supported by Portuguese national funds through FCT/MCTES (PIDDAC): CIMO UID/00690/2025 (10.54499/UID/00690/2025) and UID/PRR/00690/2025 (10.54499/UID/PRR/00690/2025); SusTEC, LA/P/0007/2020 (DOI: 10.54499/LA/P/0007/2020). G.M. thanks the Institut Universitaire de France for the Senior Chair.

REFERENCES

(1) Le, P.-A.; Trung, V. D.; Nguyen, P. L.; Bac Phung, T. V.; Natsuki, J.; Natsuki, T. The Current Status of Hydrogen Energy: An Overview. *RSC Adv.* **2023**, *13* (40), 28262−28287.

(2) International Energy Agency *The Future of Hydrogen: Seizing Today's Opportunities*; OECD: 2019

(3) Boretti, A.; Banik, B. K. Advances in Hydrogen Production from Natural Gas Reforming. *Adv. Energy Sustainable Res* **2021**, *2* (11), 2100097.

(4) Ishaq, H.; Dincer, I.; Crawford, C. A Review on Hydrogen Production and Utilization: Challenges and Opportunities. *Int. J. Hydrogen Energy* **2022**, *47* (62), 26238−26264.

(5) Brandon, N. P.; Kurban, Z. Clean Energy and the Hydrogen Economy. *Philos. Trans. R. Soc. A* **2017**, *375* (2098R), 20160400.

(6) Yang, M.; Hunger, R.; Berrettoni, S.; Sprecher, B.; Wang, B. A Review of Hydrogen Storage and Transport Technologies. *Clean Energy* **2023**, *7* (1), 190−216.

(7) Borsboom-Hanson, T.; Patlolla, S. R.; Herrera, O. E.; Mérida, W. Point-to-Point Transportation: The Economics of Hydrogen Export. *Int. J. Hydrogen Energy* **2022**, *47* (74), 31541−31550.

(8) Islam, A.; Alam, T.; Sheibley, N.; Edmonson, K.; Burns, D.; Hernandez, M. Hydrogen Blending in Natural Gas Pipelines: A Comprehensive Review of Material Compatibility and Safety Considerations. *Int. J. Hydrogen Energy* **2024**, *93*, 1429−1461.

(9) Lipiäinen, S.; Lipiäinen, K.; Ahola, A.; Vakkilainen, E. Use of Existing Gas Infrastructure in European Hydrogen Economy. *Int. J. Hydrogen Energy* **2023**, *48* (80), 31317−31329.

(10) Sholl, D. S.; Lively, R. P. Seven Chemical Separations to Change the World. *Nature* **2016**, *532* (7600), 435−437.

(11) Khalifa, O.; Alkhatib, I. I. I.; Bahamon, D.; Alhajaj, A.; Abu-Zahra, M. R. M.; Vega, L. F. Modifying Absorption Process Configurations to Improve Their Performance for Post-Combustion CO2 Capture − What Have We Learned and What Is Still Missing? *Chem. Eng. J.* **2022**, *430*, 133096.

(12) Lider, A.; Kudiiarov, V.; Kurdyumov, N.; Lyu, J.; Koptsev, M.; Travitzky, N.; Hotza, D. Materials and Techniques for Hydrogen Separation from Methane-Containing Gas Mixtures. *Int. J. Hydrogen Energy* **2023**, *48* (73), 28390−28411.

(13) Lin, R.-B.; Xiang, S.; Xing, H.; Zhou, W.; Chen, B. Exploration of Porous Metal−Organic Frameworks for Gas Separation and Purification. *Coord. Chem. Rev.* **2019**, *378*, 87−103.

(14) Luberti, M.; Ahn, H. Review of Polybed Pressure Swing Adsorption for Hydrogen Purification. *Int. J. Hydrogen Energy* **2022**, *47* (20), 10911−10933.

(15) Chen, H.; Sholl, D. S. Predictions of Selectivity and Flux for CH4/H2 Separations Using Single Walled Carbon Nanotubes as Membranes. *J. Membr. Sci.* **2006**, *269* (1−2), 152−160.

(16) Bucior, B. J.; Chen, D.-L.; Liu, J.; Johnson, J. K. Porous Carbon Nanotube Membranes for Separation of H_2/CH_4 and CO_2/CH_4 Mixtures. *J. Phys. Chem. C* **2012**, *116* (49), 25904−25910.

(17) Zhou, L.; Yang, J.; Li, G.; Wang, J.; Zhang, Y.; Lu, J.; Yin, D. Highly H 2 Permeable SAPO-34 Membranes by Steam-Assisted Conversion Seeding. *Int. J. Hydrogen Energy* **2014**, *39* (27), 14949−14954.

(18) Mei, W.; Du, Y.; Wu, T.; Gao, F.; Wang, B.; Duan, J.; Zhou, J.; Zhou, R. High-Flux CHA Zeolite Membranes for H2 Separations. *J. Membr. Sci.* **2018**, *565*, 358−369.

(19) Dakhchoune, M.; Villalobos, L. F.; Semino, R.; Liu, L.; Rezaei, M.; Schouwink, P.; Avalos, C. E.; Baade, P.; Wood, V.; Han, Y.; Ceriotti, M.; Agrawal, K. V. Gas-Sieving Zeolitic Membranes Fabricated by Condensation of Precursor Nanosheets. *Nat. Mater.* **2021**, *20* (3), 362−369.

(20) Jiang, C.; Wang, X.; Ouyang, Y.; Lu, K.; Jiang, W.; Xu, H.; Wei, X.; Wang, Z.; Dai, F.; Sun, D. Recent Advances in Metal−Organic Frameworks for Gas Adsorption/Separation. *Nanoscale Adv.* **2022**, *4* (9), 2077−2089.

(21) Li, D.; Yadav, A.; Zhou, H.; Roy, K.; Thanasekaran, P.; Lee, C. Advances and Applications of Metal-Organic Frameworks (MOFs) in Emerging Technologies: A Comprehensive Review. *Global Challenges* **2024**, *8* (2), 2300244.

(22) Suremann, N. F.; McCarthy, B. D.; Gschwind, W.; Kumar, A.; Johnson, B. A.; Hammarström, L.; Ott, S. Molecular Catalysis of Energy Relevance in Metal−Organic Frameworks: From Higher Coordination Sphere to System Effects. *Chem. Rev.* **2023**, *123* (10), 6545−6611.

(23) Yuan, H.; Li, N.; Fan, W.; Cai, H.; Zhao, D. Metal-Organic Framework Based Gas Sensors. *Adv. Sci.* **2022**, *9* (6), 2104374.

(24) Sun, Z.; Li, T.; Mei, T.; Liu, Y.; Wu, K.; Le, W.; Hu, Y. Nanoscale MOFs in Nanomedicine Applications: From Drug Delivery to Therapeutic Agents. *J. Mater. Chem. B* **2023**, *11* (15), 3273−3294.

(25) Lin, J.-B.; Nguyen, T. T. T.; Vaidhyanathan, R.; Burner, J.; Taylor, J. M.; Durekova, H.; Akhtar, F.; Mah, R. K.; Ghaffari-Nik, O.; Marx, S.; Fylstra, N.; Iremonger, S. S.; Dawson, K. W.; Sarkar, P.; Hovington, P.; Rajendran, A.; Woo, T. K.; Shimizu, G. K. H. A Scalable Metal-Organic Framework as a Durable Physisorbent for Carbon Dioxide Capture. *Science* **2021**, *374* (6574), 1464−1469.

(26) Chen, B.; Fan, D.; Pinto, R. V.; Dovgaliuk, I.; Nandi, S.; Chakraborty, D.; García-Moncada, N.; Vimont, A.; McMonagle, C. J.; Bordonhos, M.; et al. A Scalable Robust Microporous Al-MOF for Post-Combustion Carbon Capture. *Adv. Sci.* **2024**, *11* (21), 2401070.

(27) Li, W.; Shuai, Q.; Yu, J. Recent Advances of Carbon Capture in Metal−Organic Frameworks: A Comprehensive Review. *Small* **2024**, *20* (45), 2402783.

(28) Zhou, L.; Brântuas, P.; Henrique, A.; Reinsch, H.; Wahiduzzaman, M.; Grenèche, J.; Rodrigues, A. E.; Silva, J. A. C.; Maurin, G.; Serre, C. A Microporous Multi-Cage Metal−Organic Framework for an Effective One-Step Separation of Branched Alkanes Feeds. *Angew. Chem.* **2024**, *136* (15), No. e202320008.

(29) Yang, L.; Qian, S.; Wang, X.; Cui, X.; Chen, B.; Xing, H. Energy-Efficient Separation Alternatives: Metal−Organic Frameworks and Membranes for Hydrocarbon Separation. *Chem. Soc. Rev.* **2020**, *49* (15), 5359−5406.

(30) Guo, H.; Zhu, G.; Hewitt, I. J.; Qiu, S. "Twin Copper Source" Growth of Metal−Organic Framework Membrane: $Cu_3(BTC)_2$ with High Permeability and Selectivity for Recycling H_2. *J. Am. Chem. Soc.* **2009**, *131* (5), 1646−1647.

(31) Bux, H.; Liang, F.; Li, Y.; Cravillon, J.; Wiebcke, M.; Caro, J. Zeolitic Imidazolate Framework Membrane with Molecular Sieving Properties by Microwave-Assisted Solvothermal Synthesis. *J. Am. Chem. Soc.* **2009**, *131* (44), 16000−16001.

(32) Huang, A.; Caro, J. Covalent Post-Functionalization of Zeolitic Imidazolate Framework ZIF-90 Membrane for Enhanced Hydrogen Selectivity. *Angew. Chem. Int. Ed.* **2011**, *50* (21), 4979−4982.

(33) Herm, Z. R.; Krishna, R.; Long, J. R. CO2/CH4, CH4/H2 and CO2/CH4/H2 Separations at High Pressures Using Mg2(Dobdc). *Microporous Mesoporous Mater.* **2012**, *151*, 481−487.

(34) Zhang, F.; Zou, X.; Gao, X.; Fan, S.; Sun, F.; Ren, H.; Zhu, G. Hydrogen Selective NH_2 -MIL-53(Al) MOF Membranes with High Permeability. *Adv. Funct. Mater.* **2012**, *22* (17), 3583−3590.

(35) Wu, D.; Wang, C.; Liu, B.; Liu, D.; Yang, Q.; Zhong, C. Large-scale Computational Screening of Metal-organic Frameworks for CH_4/H_2 Separation. *AIChE J.* **2012**, *58* (7), 2078−2084.

(36) Basdogan, Y.; Sezginel, K. B.; Keskin, S. Identifying Highly Selective Metal Organic Frameworks for CH_4/H_2 Separations Using Computational Tools. *Ind. Eng. Chem. Res.* **2015**, *54* (34), 8479−8491.

(37) Erucar, I.; Keskin, S. Computational Assessment of MOF Membranes for CH4/H2 Separations. *J. Membr. Sci.* **2016**, *514*, 313−321.

(38) Altintas, C.; Erucar, I.; Keskin, S. High-Throughput Computational Screening of the Metal Organic Framework Database for CH_4/H_2 Separations. *ACS Appl. Mater. Interfaces* **2018**, *10* (4), 3668−3679.

(39) Altintas, C.; Avci, G.; Daglar, H.; Gulcay-Ozcan, E.; Erucar, I.; Keskin, S. Computer Simulations of 4240 MOF Membranes for H_2/CH_4 Separations: Insights into Structure−Performance Relations. *J. Mater. Chem. A* **2018**, *6* (14), 5836−5847.

https://doi.org/10.1021/acs.chemmater.5c03403
Chem. Mater. 2026, 38, 5438−5452

(40) Bai, X.; Shi, Z.; Xia, H.; Li, S.; Liu, Z.; Liang, H.; Liu, Z.; Wang, B.; Qiao, Z. Machine-Learning-Assisted High-Throughput Computational Screening of Metal−Organic Framework Membranes for Hydrogen Separation. *Chem. Eng. J.* **2022**, *446*, 136783.
(41) Li, X.-D.; Liu, C.-X.; Xie, Y.-Y.; Feng, S.-Q.; Liu, X.-Y. Machine-Learning-Assisted High-Throughput Computational Study of CH4/H2 Adsorption and Separation in Anion-Pillared MOFs. *Int. J. Hydrogen Energy* **2025**, *116*, 530−543.
(42) Sezgin, P.; Keskin, S. Integrating Molecular Simulations with Machine Learning to Discover Selective MOFs for CH_4/H_2 Separation. *J. Phys. Chem. C* **2025**, *129* (28), 13089−13099.
(43) White, A. J.; Gibaldi, M.; Burner, J.; Mayo, R. A.; Woo, T. K. High Structural Error Rates in "Computation-Ready" MOF Databases Discovered by Checking Metal Oxidation States. *J. Am. Chem. Soc.* **2025**, *147* (21), 17579−17583.
(44) Sanderson, K. World's Most Porous Sponges: Intricate Carbon-Trapping Powders Hit the Market. *Nature* **2025**, *643* (8071), 322−324.
(45) Paul, T.; Juma, A.; Alqerem, R.; Karanikolos, G.; Arafat, H. A.; Dumée, L. F. Scale-up of Metal-Organic Frameworks Production: Engineering Strategies and Prospects towards Sustainable Manufacturing. *J. Environ. Chem. Eng.* **2023**, *11* (5), 111112.
(46) Ryu, U.; Jee, S.; Rao, P. C.; Shin, J.; Ko, C.; Yoon, M.; Park, K. S.; Choi, K. M. Recent Advances in Process Engineering and Upcoming Applications of Metal−Organic Frameworks. *Coord. Chem. Rev.* **2021**, *426*, 213544.
(47) Chakraborty, D.; Yurdusen, A.; Mouchaham, G.; Nouar, F.; Serre, C. Large-Scale Production of Metal−Organic Frameworks. *Adv. Funct. Mater.* **2024**, *34* (43), 2309089.
(48) Cadiau, A.; Lee, J. S.; Damasceno Borges, D.; Fabry, P.; Devic, T.; Wharmby, M. T.; Martineau, C.; Foucher, D.; Taulelle, F.; Jun, C.; Hwang, Y. K.; Stock, N.; De Lange, M. F.; Kapteijn, F.; Gascon, J.; Maurin, G.; Chang, J.; Serre, C. Design of Hydrophilic Metal Organic Framework Water Adsorbents for Heat Reallocation. *Adv. Mater.* **2015**, *27* (32), 4775−4780.
(49) Volkringer, C.; Loiseau, T.; Haouas, M.; Taulelle, F.; Popov, D.; Burghammer, M.; Riekel, C.; Zlotea, C.; Cuevas, F.; Latroche, M.; Phanon, D.; Knöfelv, C.; Llewellyn, P. L.; Férey, G. Occurrence of Uncommon Infinite Chains Consisting of Edge-Sharing Octahedra in a Porous Metal Organic Framework-Type Aluminum Pyromellitate $Al_4(OH)_8[C_{10}O_8H_2]$ (MIL-120): Synthesis, Structure, and Gas Sorption Properties. *Chem. Mater.* **2009**, *21* (24), 5783−5791.
(50) Chevreau, H.; Permyakova, A.; Nouar, F.; Fabry, P.; Livage, C.; Ragon, F.; Garcia-Marquez, A.; Devic, T.; Steunou, N.; Serre, C.; Horcajada, P. Synthesis of the Biocompatible and Highly Stable MIL-127(Fe): From Large Scale Synthesis to Particle Size Control. *CrystEngComm* **2016**, *18* (22), 4094−4101.
(51) Groom, C. R.; Bruno, I. J.; Lightfoot, M. P.; Ward, S. C. The Cambridge Structural Database. *Acta Crystallogr., Sect. B: Struct. Sci., Cryst. Eng. Mater.* **2016**, *72* (2), 171−179.
(52) Kresse, G.; Furthmüller, J. Efficient Iterative Schemes for *Ab Initio* Total-Energy Calculations Using a Plane-Wave Basis Set. *Phys. Rev. B* **1996**, *54* (16), 11169−11186.
(53) Perdew, J. P.; Burke, K.; Ernzerhof, M. Generalized Gradient Approximation Made Simple. *Phys. Rev. Lett.* **1996**, *77* (18), 3865−3868.
(54) Grimme, S. Semiempirical GGA-type Density Functional Constructed with a Long-range Dispersion Correction. *J. Comput. Chem.* **2006**, *27* (15), 1787−1799.
(55) Grimme, S.; Ehrlich, S.; Goerigk, L. Effect of the Damping Function in Dispersion Corrected Density Functional Theory. *J. Comput. Chem.* **2011**, *32* (7), 1456−1465.
(56) Blöchl, P. E. Projector Augmented-Wave Method. *Phys. Rev. B* **1994**, *50* (24), 17953−17979.
(57) Monkhorst, H. J.; Pack, J. D. Special Points for Brillouin-Zone Integrations. *Phys. Rev. B* **1976**, *13* (12), 5188−5192.
(58) Willems, T. F.; Rycroft, C. H.; Kazi, M.; Meza, J. C.; Haranczyk, M. Algorithms and Tools for High-Throughput Geometry-Based Analysis of Crystalline Porous Materials. *Microporous Mesoporous Mater.* **2012**, *149* (1), 134−141.
(59) Dutta, P. *MOF Structures and Adsorption Isotherms for Methane/Hydrogen Separation*; https://github.com/prantardutta/MOF-Methane-Hydrogen.
(60) Martin, M. G.; Siepmann, J. I. Transferable Potentials for Phase Equilibria. 1. United-Atom Description of *n* -Alkanes. *J. Phys. Chem. B* **1998**, *102* (14), 2569−2577.
(61) Buch, V. Path Integral Simulations of Mixed *Para* -D2 and *Ortho* -D2 Clusters: The Orientational Effects. *J. Chem. Phys.* **1994**, *100* (10), 7610−7629.
(62) Barraco, M.; Neyertz, S.; Benes, N. E.; Brown, D. Comparison of Eight Classical Lennard-Jones-Based H_2 Molecular Models in the Gas Phase at Temperatures and Pressures Relevant to Hydrogen On-Board Storage Tanks. *J. Phys. Chem. A* **2023**, *127* (30), 6335−6346.
(63) Darkrim, F.; Levesque, D. High Adsorptive Property of Opened Carbon Nanotubes at 77 K. *J. Phys. Chem. B* **2000**, *104* (29), 6773−6776.
(64) Tanaka, H.; Kanoh, H.; Yudasaka, M.; Iijima, S.; Kaneko, K. Quantum Effects on Hydrogen Isotope Adsorption on Single-Wall Carbon Nanohorns. *J. Am. Chem. Soc.* **2005**, *127* (20), 7511−7516.
(65) Rappe, A. K.; Casewit, C. J.; Colwell, K. S.; Goddard, W. A.; Skiff, W. M. UFF, a Full Periodic Table Force Field for Molecular Mechanics and Molecular Dynamics Simulations. *J. Am. Chem. Soc.* **1992**, *114* (25), 10024−10035.
(66) Yang, Q.; Zhong, C. Molecular Simulation of Carbon Dioxide/Methane/Hydrogen Mixture Adsorption in Metal−Organic Frameworks. *J. Phys. Chem. B* **2006**, *110* (36), 17776−17783.
(67) Vlugt, T. J. H.; García-Pérez, E.; Dubbeldam, D.; Ban, S.; Calero, S. Computing the Heat of Adsorption Using Molecular Simulations: The Effect of Strong Coulombic Interactions. *J. Chem. Theory Comput.* **2008**, *4* (7), 1107−1118.
(68) Horn, H. W.; Swope, W. C.; Pitera, J. W.; Madura, J. D.; Dick, T. J.; Hura, G. L.; Head-Gordon, T. Development of an Improved Four-Site Water Model for Biomolecular Simulations: TIP4P-Ew. *J. Chem. Phys.* **2004**, *120* (20), 9665−9678.
(69) Wells, B. A.; Chaffee, A. L. Ewald Summation for Molecular Simulations. *J. Chem. Theory Comput.* **2015**, *11* (8), 3684−3695.
(70) Olson, D. H. Reinvestigation of the Crystal Structure of the Zeolite Hydrated NaX. *J. Phys. Chem.* **1970**, *74* (14), 2758−2764.
(71) Zhu, L.; Seff, K. Reinvestigation of the Crystal Structure of Dehydrated Sodium Zeolite X. *J. Phys. Chem. B* **1999**, *103* (44), 9512−9518.
(72) Maurin, G.; Llewellyn, P. L.; Bell, R. G. Adsorption Mechanism of Carbon Dioxide in Faujasites: Grand Canonical Monte Carlo Simulations and Microcalorimetry Measurements. *J. Phys. Chem. B* **2005**, *109* (33), 16084−16091.
(73) Wender, A.; Barreau, A.; Lefebvre, C.; Di Lella, A.; Boutin, A.; Ungerer, P.; Fuchs, A. H. Adsorption of N-Alkanes in Faujasite Zeolites: Molecular Simulation Study and Experimental Measurements. *Adsorption* **2007**, *13* (5−6), 439−451.
(74) Martin-Calvo, A.; Gutiérrez-Sevillano, J. J.; Parra, J. B.; Ania, C. O.; Calero, S. Transferable Force Fields for Adsorption of Small Gases in Zeolites. *Phys. Chem. Chem. Phys.* **2015**, *17* (37), 24048−24055.
(75) Cavenati, S.; Grande, C. A.; Rodrigues, A. E. Adsorption Equilibrium of Methane, Carbon Dioxide, and Nitrogen on Zeolite 13X at High Pressures. *J. Chem. Eng. Data* **2004**, *49* (4), 1095−1101.
(76) Streb, A.; Mazzotti, M. Adsorption for Efficient Low Carbon Hydrogen Production: Part 1—Adsorption Equilibrium and Breakthrough Studies for H2/CO2/CH4 on Zeolite 13X. *Adsorption* **2021**, *27* (4), 541−558.
(77) Luo, J.; Said, O. B.; Xie, P.; Gibaldi, M.; Burner, J.; Pereira, C.; Woo, T. K. MEPO-ML: A Robust Graph Attention Network Model for Rapid Generation of Partial Atomic Charges in Metal-Organic Frameworks. *Npj Comput. Mater.* **2024**, *10* (1), 224.
(78) Nosé, S. A Unified Formulation of the Constant Temperature Molecular Dynamics Methods. *J. Chem. Phys.* **1984**, *81* (1), 511−519.
(79) Hoover, W. G. Canonical Dynamics: Equilibrium Phase-Space Distributions. *Phys. Rev. A* **1985**, *31* (3), 1695−1697.

https://doi.org/10.1021/acs.chemmater.5c03403
Chem. Mater. 2026, 38, 5438−5452

(80) Thompson, A. P.; Aktulga, H. M.; Berger, R.; Bolintineanu, D. S.; Brown, W. M.; Crozier, P. S.; In't Veld, P. J.; Kohlmeyer, A.; Moore, S. G.; Nguyen, T. D.; et al. LAMMPS - a flexible simulation tool for particle-based materials modeling at the atomic, meso, and continuum scales. *Comput. Phys. Commun.* **2022**, *271*, 108171.
(81) Permyakova, A.; Skrylnyk, O.; Courbon, E.; Affram, M.; Wang, S.; Lee, U.; Valekar, A. H.; Nouar, F.; Mouchaham, G.; Devic, T.; De Weireld, G.; Chang, J.; Steunou, N.; Frère, M.; Serre, C. Synthesis Optimization, Shaping, and Heat Reallocation Evaluation of the Hydrophilic Metal−Organic Framework MIL-160(Al). *ChemSusChem* **2017**, *10* (7), 1419−1426.
(82) Severino, M. I.; Gkaniatsou, E.; Nouar, F.; Pinto, M. L.; Serre, C. MOFs Industrialization: A Complete Assessment of Production Costs. *Faraday Discuss.* **2021**, *231*, 326−341.
(83) Wang, M.; Guo, H.; Wang, C.; Xiong, L.; Chen, X.; Peng, F.; Yao, S.; Li, H.; Zhang, H.; Chen, X. Scale-up Synthesis and Shaping of MIL-160(Al) Applicable for Efficient CO2 Adsorption and Separation. *Sep. Purif. Technol.* **2025**, *360*, 131091.
(84) Sesé, L. M. Study of the Feynman-Hibbs Effective Potential against the Path-Integral Formalism for Monte Carlo Simulations of Quantum Many-Body Lennard-Jones Systems. *Mol. Phys.* **1994**, *81* (6), 1297−1312.
(85) Liu, S.; Dupuis, R.; Fan, D.; Benzaria, S.; Bonneau, M.; Bhatt, P.; Eddaoudi, M.; Maurin, G. Machine Learning Potential for Modelling H_2 Adsorption/Diffusion in MOFs with Open Metal Sites. *Chem. Sci.* **2024**, *15* (14), 5294−5302.
(86) Severino, M. I.; Al Mohtar, A.; Soares, C. V.; Kolmykov, O.; Freitas, C.; Dovgaliuk, I.; Martineau, C.; Pimenta, V.; Nouar, F.; Maurin, G.; Pinto, M. L.; Serre, C. Hydrophobic MOFs for the Efficient Capture of Highly Polar Volatile Organic Compound. *J. Mater. Chem. A* **2023**, *11* (8), 4238−4247.
(87) Gopalsamy, K.; Fan, D.; Naskar, S.; Magnin, Y.; Maurin, G. Engineering of an Isoreticular Series of CALF-20 Metal−Organic Frameworks for CO_2 Capture. *ACS Appl. Eng. Mater.* **2024**, *2* (1), 96−103.
(88) Reinsch, H.; Van Der Veen, M. A.; Gil, B.; Marszalek, B.; Verbiest, T.; De Vos, D.; Stock, N. S. Sorption Characteristics, and Nonlinear Optical Properties of a New Series of Highly Stable Aluminum MOFs. *Chem. Mater.* **2013**, *25* (1), 17−26.
(89) Yang, Q.; Vaesen, S.; Vishnuvarthan, M.; Ragon, F.; Serre, C.; Vimont, A.; Daturi, M.; De Weireld, G.; Maurin, G. Probing the Adsorption Performance of the Hybrid Porous MIL-68(Al): A Synergic Combination of Experimental and Modelling Tools. *J. Mater. Chem.* **2012**, *22* (20), 10210.
(90) Reinsch, H.; Homburg, T.; Heidenreich, N.; Fröhlich, D.; Hennninger, S.; Wark, M.; Stock, N. Green Synthesis of a New Al-MOF Based on the Aliphatic Linker Mesaconic Acid: Structure, Properties and In Situ Crystallisation Studies of Al-MIL-68-Mes. *Chem.-Eur. J.* **2018**, *24* (9), 2173−2181.
(91) Wang, S.; Xhaferaj, N.; Wahiduzzaman, M.; Oyekan, K.; Li, X.; Wei, K.; Zheng, B.; Tissot, A.; Marrot, J.; Shepard, W.; Martineau-Corcos, C.; Filinchuk, Y.; Tan, K.; Maurin, G.; Serre, C. Engineering Structural Dynamics of Zirconium Metal−Organic Frameworks Based on Natural C4 Linkers. *J. Am. Chem. Soc.* **2019**, *141* (43), 17207−17216.
(92) Guillerm, V.; Ragon, F.; Dan-Hardi, M.; Devic, T.; Vishnuvarthan, M.; Campo, B.; Vimont, A.; Clet, G.; Yang, Q.; Maurin, G.; Férey, G.; Vittadini, A.; Gross, S.; Serre, C. A Series of Isoreticular, Highly Stable, Porous Zirconium Oxide Based Metal−Organic Frameworks. *Angew. Chem. Int. Ed.* **2012**, *51* (37), 9267−9271.
(93) Matemb Ma Ntep, T. J.; Wahiduzzaman, M.; Laurenz, E.; Cornu, I.; Mouchaham, G.; Dovgaliuk, I.; Nandi, S.; Knop, K.; Jansen, C.; Nouar, F.; et al. When Polymorphism in Metal−Organic Frameworks Enables Water Sorption Profile Tunability for Enhancing Heat Allocation and Water Harvesting Performance. *Adv. Mater.* **2024**, *36* (12), 2211302.
(94) Ruthven, D. M. *Principles of Adsorption and Adsorption Processes*; Wiley: New York, 1984.
(95) Reimer, N.; Reinsch, H.; Inge, A. K.; Stock, N. New Al-MOFs Based on Sulfonyldibenzoate Ions: A Rare Example of Intralayer Porosity. *Inorg. Chem.* **2015**, *54* (2), 492−501.
(96) Gosch, J.; Guiotto, V.; Steinke, F.; Svensson Grape, E.; Atzori, C.; Mertin, K.; Otto, T.; Ruser, N.; Meier, C.; Morelli Venturi, D.; Inge, A. K.; Lomachenko, K. A.; Crocellà, V.; Stock, N. Discovery and In Situ Crystallization Studies of Cerium-Based Metal−Organic Frameworks with V-Shaped Linker Molecules. *Inorg. Chem.* **2023**, *62* (51), 20929−20939.
(97) Poschmann, M. P. M.; Reinsch, H.; Stock, N. $[M_2(\mu\text{-}OH)_2(DHBQ)_3]$ (M = Zr, Hf) - Two New Isostructural Coordination Polymers Based on the Unique M_2O_{14} Inorganic Building Unit and 2,5-Dioxido-*p*-benzoquinone as Linker Molecule. *Z. Anorg. Allg. Chem.* **2021**, *647* (5), 436−441.
(98) Fu, R.; Huang, X.; Hu, S.; Xiang, S.; Wu, X. Rational Design of New Bright Luminescent Zinc Diphosphonates with 12-Member Ring Channels. *Inorg. Chem.* **2006**, *45* (14), 5254−5256.
(99) Landrum, G.; Tosco, P.; Kelley, B.; Rodriguez, R.; Cosgrove, D.; Vianello, R.; Sriniker, P. G.; Jones, G.; Kawashima, E.; NadineSchneider, D. N.; et al. *Rdkit/Rdkit: 2025_09_2 (Q3 2025) Release*; Zenodo, 2025. .
(100) Verstreken, M. F. K.; Chanut, N.; Magnin, Y.; Landa, H. O. R.; Denayer, J. F. M.; Baron, G. V.; Ameloot, R. Mind the Gap: The Role of Mass Transfer in Shaped Nanoporous Adsorbents for Carbon Dioxide Capture. *J. Am. Chem. Soc.* **2024**, *146* (34), 23633−23648.
(101) Zheng, Z.; Alawadhi, A. H.; Yaghi, O. M. Green Synthesis and Scale-Up of MOFs for Water Harvesting from Air. *Mol. Front. J.* **2023**, *7* (1n02), 20−39.
(102) Solovyeva, M. V.; Shkatulov, A. I.; Gordeeva, L. G.; Fedorova, E. A.; Krieger, T. A.; Aristov, Y. I. Water Vapor Adsorption on CAU-10- *X*: Effect of Functional Groups on Adsorption Equilibrium and Mechanisms. *Langmuir* **2021**, *37* (2), 693−702.
(103) Grigoletto, S.; Karami, K.; Maye, I.; Padunnappattu, A.; Ravichandran, S.; Wahiduzzaman, M.; Vanduyfhuys, L.; Van Speybroeck, V.; Thommes, M.; Denayer, J. F. M.; Stock, N.; Maurin, G. High-Performance Hydrophobic MOFs for Selective Acetone Capture under Humid Conditions. *J. Mater. Chem. A* **2025**, *13* (32), 26401−26412.

https://doi.org/10.1021/acs.chemmater.5c03403
Chem. Mater. 2026, 38, 5438−5452